

## Research Paper

## Numerical simulations of triaxial compression tests of cemented sandstone

Aigerim K. Rakhimzhanova<sup>a,\*</sup>, Colin Thornton<sup>b</sup>, Nguyen Hop Minh<sup>c</sup>, Sai Cheong Fok<sup>a</sup>, Yong Zhao<sup>a</sup>

<sup>a</sup> Nazarbayev University, Astana 010000, Kazakhstan

<sup>b</sup> University of Birmingham, Edgbaston, Birmingham B15 2TT, UK

<sup>c</sup> Fulbright University Vietnam, Ho Chi Minh City 700000, Viet Nam

## ARTICLE INFO

## Keywords:

Discrete element method  
Contact model  
Cemented sand

## ABSTRACT

Three-dimensional DEM simulations of triaxial compression tests of cemented sandstone samples have been performed at different values of confining pressure, initial density and bond strength. The results show that with increase in bond strength, initial density and confining pressure both the initial stiffness and peak strength increase. For a higher bond strength and initial density the samples exhibit a higher rate of dilation. Bond breakage was found to increase with confining pressure and decrease with bond strength and initial density. The Mohr-Coulomb strength parameters  $c'$  and  $\phi'$  were obtained for the numerical samples and correlations between the shear strength parameters and the bond strength were established. The correlations were then used to find the value of the bond strength to be used for comparisons with results of experimental triaxial tests. The stress-strain responses of the numerical samples were found to be in good agreement with the experimental results. The critical state lines (CSL) of triaxial compression tests for both loose and medium dense systems show that the critical void ratio is independent of the initial density but increases with increase in bond strength. Increasing the bond strength increases the dilation, which leads to a higher critical state void ratio.

## 1. Introduction

Cemented sandstones hold more than 60% of the world's oil and gas fields. The materials in a sandstone reservoir are composed mainly of quartz, feldspars, mica, rock fragments and various mineral grains bound together with clay, silica or some type of cement, Bjorlykke [1]. Compared with other reservoir rocks it has a relatively high porosity of about 15% and permeability of 25–100 Darcies, which makes it the best sedimentary rock for the accumulation of hydrocarbons. The small presence of cementation influences and enriches the mechanical behaviour of the cemented sand materials. Over the past forty years, a number of researchers have studied natural and artificial cemented sandstones and carbonate sands using experimental triaxial tests [2–14].

In the last decade, bonded granular material has been numerically studied using the Discrete Element Model (DEM) proposed by Cundall and Strack [15]. Wang and Leung [11], both experimentally and numerically (2D), examined the material behaviour of cemented sand using triaxial compression tests; Jung et al. [16] numerically (3D) studied the stress-strain response of hydrate-bearing sand. Utili and Nova [17] presented a 2D contact model for bonded granular materials

based on the Mohr-Coulomb failure criteria; Obermayr et al. [18] proposed a 3D bonded-particle model for cemented sand, in which the spherical particles are connected by elastic beams; Shen et al. [19] presented a 3D bonded contact model and its application to cemented sand and to grain-coating type methane hydrate bearing sand, Shen and Jiang [20].

The aim of the present study is to carry out 3D simulations of triaxial compression tests of cemented sandstone on loose and medium dense systems in order to examine the effect of bond strength on the macro-and micro- response. Results are compared with findings from the laboratory triaxial compression tests on reservoir analogue sandstone samples from the Ustyurt-Buzachi Sedimentary Basin studied by Shabdirova et al. [21].

This journal paper is the extension of the work reported by Rakhimzhanova et al. [22] and it is divided into five parts. In Section 2, the contact models used for bonded and unbonded particles are introduced. The details of numerical simulations of triaxial compression tests are explained in Section 3. The numerical results are presented in Section 4 and some concluding remarks are provided in Section 5.

\* Corresponding author.

E-mail address: [aigerim.rakhimzhanova@nu.edu.kz](mailto:aigerim.rakhimzhanova@nu.edu.kz) (A.K. Rakhimzhanova).

## 2. Contact models

As a result of the relative displacements between particles, forces are generated at the inter-particle contacts. The contact force-displacement behavior depends on the material properties of the particles, the sizes of the two particles in contact and the surface conditions. Contact behaviour includes all the complex variety of surface physics, including adhesion, friction, and elasticity usually all interacting at the same time in a complex geometrical arrangement, Thornton [23].

The normal and tangential stiffnesses for frictional elastic spheres without adhesion at the contact are described by the theories of Hertz [24], and Mindlin [25], respectively. For two spheres of radii  $R_i$  and elastic properties  $E_i$ ,  $G_i$  and  $\nu_i$  ( $i = 1, 2$ ), the theory of Hertz relates the normal force  $F_n$  to the relative approach  $\alpha$  of the centres of the two contiguous spheres.

$$F_n = \frac{4}{3}E^*\sqrt{R^*}\alpha^3 \quad (1)$$

where

$$\frac{1}{R^*} = \frac{1}{R_1} + \frac{1}{R_2} \quad (2)$$

and

$$\frac{1}{E^*} = \frac{1 - \nu_1^2}{E_1} + \frac{1 - \nu_2^2}{E_2} \quad (3)$$

From the above, the normal contact stiffness is

$$k_n = 2E^*\sqrt{R^*}\alpha \quad (4)$$

The tangential force is calculated incrementally and depends on whether the normal force is increasing or decreasing, see Thornton [23]. The tangential force at the  $i$ th timestep is obtained from

$$F_t^i = F_t^{i-1} + k_t^i \Delta \delta \text{ if } \Delta F_n \geq 0 \quad (5a)$$

or

$$F_t^i = F_t^{i-1} \left( \frac{k_t^i}{k_t^{i-1}} \right) + k_t^i \Delta \delta \text{ if } \Delta F_n < 0 \quad (5b)$$

$$\text{except if } F_t \geq \mu F_n \text{ then } F_t = \mu F_n \quad (5c)$$

The contact stiffness is defined by

$$k_t = 8G^*\sqrt{R^*}\alpha \quad (6)$$

which is the Mindlin [25] 'no-slip' solution, where

$$\frac{1}{G^*} = \frac{2 - \nu_1}{G_1} + \frac{2 - \nu_2}{G_2} \quad (7)$$

The normal and tangential damping forces are:

$$F_{nd} = 2\beta\sqrt{m^*k_n}\Delta\alpha/\Delta t \quad (8)$$

and

$$F_{td} = 2\beta\sqrt{m^*k_t}\Delta\delta/\Delta t \quad (9)$$

where

$$\beta = \frac{\text{frac}}{2\pi \cdot \text{freq}} \quad (10)$$

with the Rayleigh damping parameters chosen to be fraction = 0.05 and frequency = 0.5. However, following Cundall and Strack [15], the contact damping forces do not contribute to the stored contact forces, only to the out-of-balance force on the particle, from which the particle acceleration is obtained.

The so-called JKR model of adhesion was proposed by Johnson et al. [26] to model auto-adhesive interactions due to van der Waals forces between silt sized particles. However, the oil field reservoir rock is sandstone, i.e. sand with cement bonds. Nevertheless, we used a simple

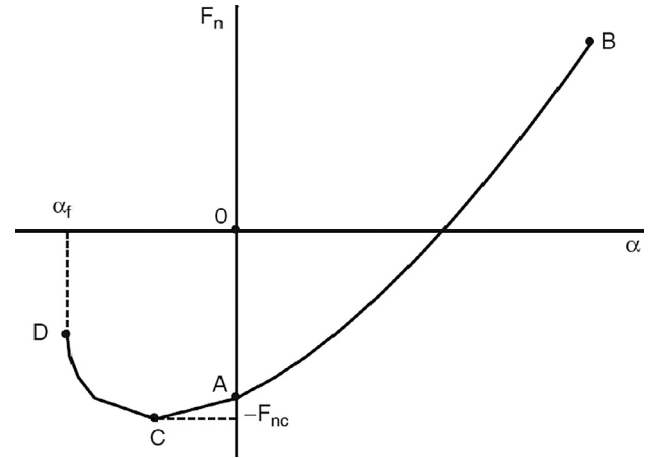


Fig. 1. Normal force-displacement curve for JKR theory.

modification of the JKR model for the normal contact force and the Mindlin [25] no slip model for the tangential contact force. The relationship between the normal contact force  $F_n$  and the relative approach  $\alpha$  was provided by Johnson [27] and is given below, and illustrated in Fig. 1.

$$\frac{\alpha}{\alpha_f} = \frac{3\left(\frac{F_n}{F_{nc}}\right) + 2 + 2\left(1 + \frac{F_n}{F_{nc}}\right)^{1/2}}{3^{2/3}\left[\frac{F_n}{F_{nc}} + 2 + 2\left(1 + \frac{F_n}{F_{nc}}\right)^{1/2}\right]^{1/3}} \quad (11)$$

where

$$\alpha_f = \left( \frac{3F_{nc}^2}{16R^*E^{*2}} \right)^{1/3} \quad (12)$$

is the relative approach (negative) at which the contact breaks, point D in Fig. 1.

When two particles come into contact ( $\alpha = 0$ ), the normal force  $F_n$  immediately drops down to point A due to van der Waals attractive forces, where  $F_n = -8F_{nc}/9$ . During the compression (loading stage) the normal contact force increases from point A to say point B. If decompression (unloading) then occurs the response is elastic and the force returns from point B to point A, where the value of relative approach is  $\alpha = 0$ , but there is still a finite area of contact. All the work that was done during the loading stage will be recovered when the normal contact force reaches point A during unloading. At point A, the spheres remain adhered together and extra work is required to break the contact. During the extra work, the tensile force increases from point A to point C and then decreases until contact breaks at point D, when  $F_n = -5F_{nc}/9$  and  $\alpha = -\alpha_f$ .

Cement bonds are not as stretchable and break in a brittle manner. Consequently, in the modified JKR model used in this research the bond breaks at point C, where  $F_n = -F_{nc}$  and  $\alpha = -\alpha_f/3^{2/3}$ . At point C, the maximum tensile force required to break the contact is:

$$F_{nc} = 1.5\pi\Gamma R^* \quad (13)$$

where  $\Gamma$  is the work of adhesion and  $\Gamma = \gamma_1 + \gamma_2$  where  $\gamma_1$  and  $\gamma_2$  are the surface energies of the two solids i.e.  $\Gamma = 2\gamma$  and  $1/R^*$  is the relative curvature of the contact.

If any new contacts are made during shear these are treated as elastic with the normal and tangential forces calculated using Eqs. (1) and (5).

## 3. Numerical simulations

The particle size distribution (PSD) data of the sandstone analogue samples from the Ustyurt-Buzachi Sedimentary Basin measured by Qicpic dynamic image analyser, Shabdirova et al. [21] was replicated

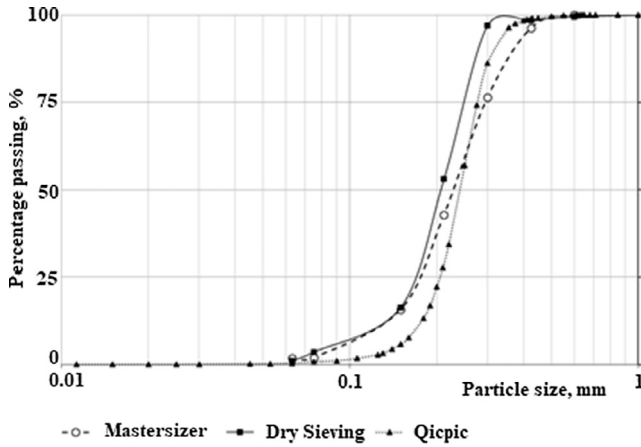


Fig. 2. Particle Size Distribution of the reservoir sand from the Ustyurt-Buzachi Sedimentary Basin.

with the numerical samples (Fig. 2).

Three-dimensional simulations of triaxial compression tests, using periodic boundaries, have been performed using 5206 spheres at different values of confining pressure and bond strength. Following Calvetti and Nova [28], the spheres were prevented from rotating in order to obtain reasonable values of shear strength.

The current simulation work is aimed to study the effects of initial density, bond strength and confining pressure on the cemented sandstone. A total of 40 simulations of triaxial compression tests on loose and medium dense samples were performed over a range of confining pressures of 100, 300, 500 and 1000 kPa and bond strengths (interface energy of adhesion) of  $\Gamma = 0, 10, 20, 30$  and  $40 \text{ J/m}^2$ , where  $\Gamma = 0 \text{ J/m}^2$  is an ‘uncemented’ sample. The simulations were divided into three stages: particle generation, isotropic and triaxial compression.

### 3.1. Particle generation

Eight different particle sizes of the sandstone analogue samples from the Ustyurt-Buzachi Sedimentary Basin were selected and randomly generated as a granular gas within a cuboidal cell of dimension 4.25 mm: 0.15 mm (614), 0.18 mm (911), 0.2 mm (783), 0.22 mm (811), 0.25 mm (1027), 0.275 mm (583), 0.3 mm (318) and 0.355 mm (159). The following mechanical properties were used for all particles: Young’s modulus  $E = 70 \text{ GPa}$ , Poisson’s ratio  $\nu = 0.3$  and experimental particle density  $\rho = 2605 \text{ kg/m}^3$ . The particle density is scaled up by a factor of  $10^{12}$  in order to model quasi-static simulations within a reasonable timescale. Thornton [29] reported that the particle density scaling does not affect forces and displacements and hence stresses and strains; the velocities and accelerations are reduced by orders of magnitude but these are not of concern when considering quasi-static behaviour. In all DEM simulations reported in this paper no gravity field is applied.

Da Cruz et al (2005) suggested that the inertial number  $I$  can be used to demonstrate whether simulations are quasi-static or not. They suggested that  $I < 1.10^{-3}$  guarantees that the simulations are quasi-static. For all the simulations presented in the paper the axial strain rate was 0.0001. The average particle diameter was 0.24 mm and the particle density used was  $2.605 \cdot 10^{15} \text{ kg/m}^3$ . Using  $I = \dot{\epsilon} d_p \sqrt{\rho/p}$ , the inertial number is calculated as  $1.10^{-3}$  for  $p = 1000 \text{ kPa}$  and  $3 \cdot 10^{-3}$  for  $p = 100 \text{ kPa}$ . Consequently, it can be argued that the simulations are approximately quasi-static.

The interparticle friction coefficient was set to  $\mu = 0.3$  and  $\mu = 0.1$  during the particle generation stage in order to obtain the loose and medium dense samples, respectively.

### 3.2. Isotropic and triaxial compression

Initially the generated sample was isotropically compressed to 10 kPa using one million timesteps. This ensured that the void ratio was constant, the mean stress was constant and the number of contacts was constant with a mechanical coordination number  $Z_m > 4$ . Having established a stable system at 10 kPa further isotropic compression was performed until 80 kPa, during which all contact interactions were calculated using the Hertz-Mindlin contact model. At 80 kPa the interparticle friction coefficient was reset to  $\mu = 0.3$  for the medium dense system and then different bond strengths were introduced for both the loose and medium dense samples. The initial number of bonds was equal to 7526 and 12,225 for all loose and medium dense samples, respectively. All contact interactions during the isotropic and triaxial compression simulations were calculated using the modified JKR model for bonded contacts but for any subsequent new contacts that may be created the Hertzian model was applied. At the start of the triaxial compression stage, the void ratio of the loose and medium dense systems were equal to 0.698 and 0.617, respectively. Numerical servo-control algorithms were used to control the isotropic compression stage and to maintain  $\sigma_3 = \sigma_2$  constant during the shear stage [29].

## 4. Numerical results

Fig. 3 shows the deviator stress vs. axial strain curves obtained for triaxial compression test simulations for both the loose and medium dense samples at a confining stress of 300 kPa. The results show that the stress-strain behaviour of cemented sand is strongly dependent on the bond strength and compared with uncemented sand is initially stiff. With increase in bond strength, both the initial stiffness and peak strength increase; and for a higher bond strength the peak stress is reached at a lower axial strain. Fig. 4 shows the effect of bond strength on the evolution of volumetric strain. All loose samples first contracted and then started to dilate, while medium dense samples only dilated. For a higher bond strength, the material starts to expand at a lower axial strain and, with increase in bond strength, the sample exhibits a higher rate of dilation. Similar behaviour has been reported for naturally and artificially cemented sands and carbonate soils [2,3,5,6,7,8,9,10,11,12,14] and numerically captured by Jung et al. [16]; Obermayr et al. [18]; Shen et al. [19]; Wang and Leung [11].

It can be seen from Figs. 3 and 4 that the mechanical response of cemented sands depends not only on the bond strength, but also on the initial density. Increasing density leads to increases in peak strength and initial stiffness; and volumetric dilation, Clough et al. [2]; Huang and Airey [7]; Rios et al. [14]. It was observed that with increase in the initial density the stress reaches a peak at a lower axial strain. All numerical loose samples reached the peak strength at about 15% axial

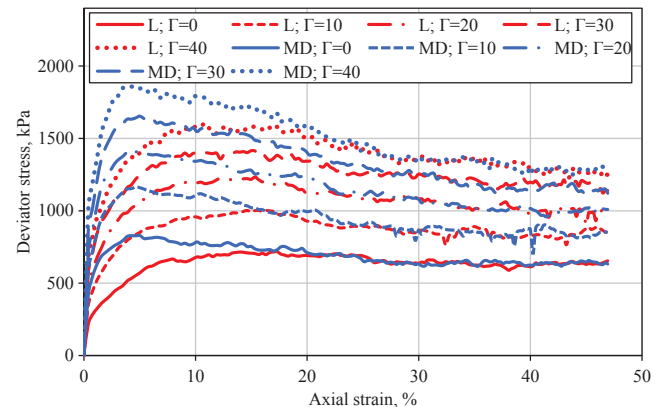


Fig. 3. The effect of bond strength on the evolution of the deviator stress for loose and medium dense samples.

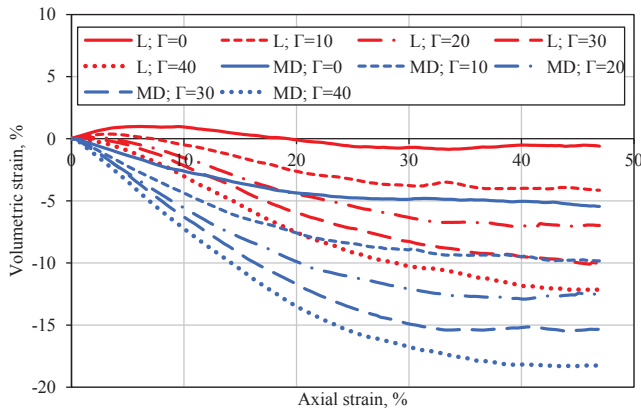


Fig. 4. The effect of bond strength on the evolution of the volumetric strain for loose and medium dense samples (at 300 kPa).

strain but for the medium dense samples peak strength occurred at less than 5% axial strain. The post-peak response of samples also depends on the bond strength and initial density. The medium dense samples show significant strain softening behaviour. It can be seen from Fig. 3 that after peak, the deviator stress for different values of bond strength gradually reduces but do not converge with the curve for ‘uncemented’ ( $\Gamma = 0$ ) sand. This is because the critical state strength depends on the magnitude of the bond strength, in the same way that it depends on the value of interparticle friction. But for a given value of  $\Gamma$  both the loose and medium dense systems reach the same critical state strength.

Figs. 5 and 6 show the evolution of the number of bonds and the number of contacts, respectively. It can be seen from Fig. 5 that the number of bonds decreases at a decreasing rate and more bonds are broken for a lower bond strength. For the bond strength value  $\Gamma = 10 \text{ J/m}^2$  all the bonded contacts have broken at 30% axial strain for both the loose and medium dense samples, while for a higher bond strength value of  $\Gamma = 40 \text{ J/m}^2$  some bonded contacts could survive. Fig. 6 shows that the total number of contacts reduces with increase in bond strength. Fig. 5 shows that, for  $\Gamma > 0$ , the number of contacts initially decreases due to the breaking of bonds but then the total number of contacts (both bonded and unbonded new contacts) increases at a decreasing rate. The results shown in Figs. 3, 4, 5 and 6 are qualitatively consistent with all of the data obtained from all of the tests simulated at other confining stresses.

Figs. 7 and 8 show the effect of confining pressure on the evolution of the deviator stress and volumetric strain, respectively, for loose and medium dense samples with a bond strength value of  $\Gamma = 20 \text{ J/m}^2$ . The results show that both the stiffness and peak strength increase with increasing confining pressure (frictional response); and higher volumetric dilation occurs at lower confining pressure levels, Clough et al.,

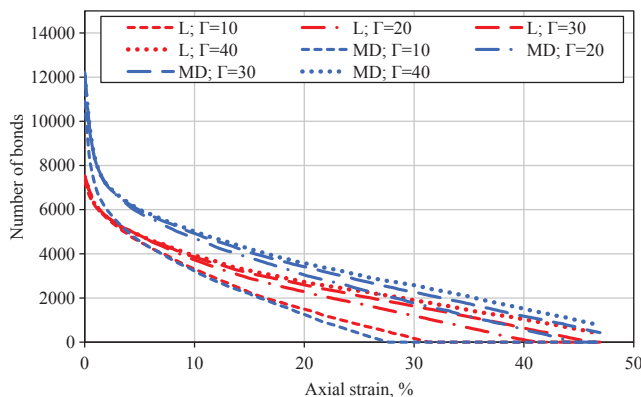


Fig. 5. Evolution of number of bonds for loose and medium dense samples (at 300 kPa).

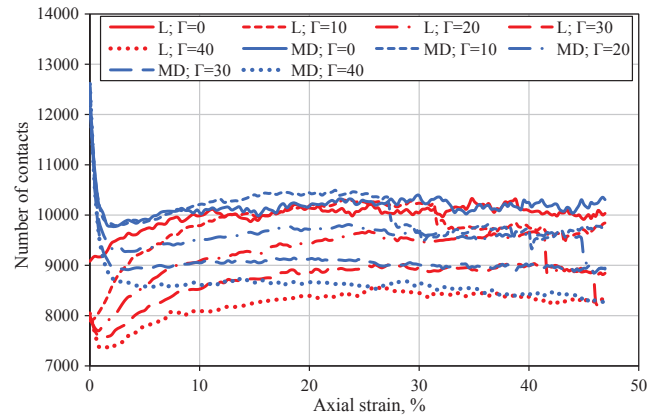


Fig. 6. Evolution of number of contacts for loose and medium dense samples (at 300 kPa).

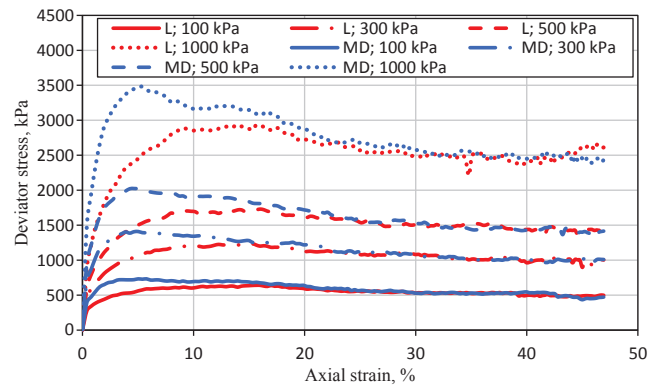


Fig. 7. The effect of confining pressure on the evolution of the deviator stress for loose and medium dense samples ( $\Gamma = 20 \text{ J/m}^2$ ).

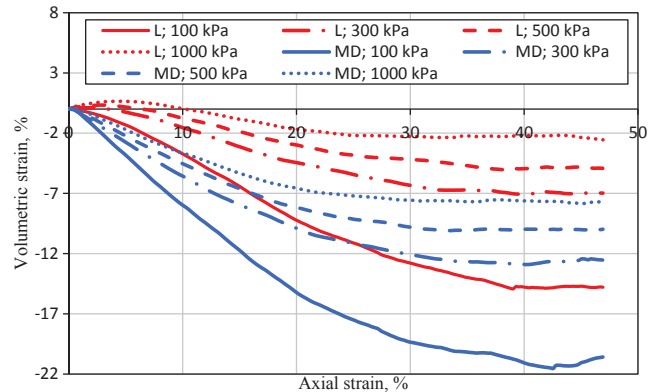


Fig. 8. The effect of confining pressure on the evolution of the volumetric strain for loose and medium dense samples ( $\Gamma = 20 \text{ J/m}^2$ ).

[2]; Lade and Overton [3]; Cucovillo and Coop, [8]. With an increase in initial density, the axial strain at failure decreases and strong volumetric dilation occurs. The stresses reached the peak state at the same axial strains for a given initial density for all confining pressures and bond strengths (loose samples at 15% of axial strain and the medium dense samples at less than 5% axial strain). The post-peak response is dependent on confining pressure, bond strength and initial density. The medium dense samples demonstrate strain softening behavior at all confining pressures.

Fig. 9 shows the effect of confining pressure on the number of bonds for loose and medium dense samples with a bond strength value of  $\Gamma = 20 \text{ J/m}^2$ . It can be seen from the figure, that significant and rapid

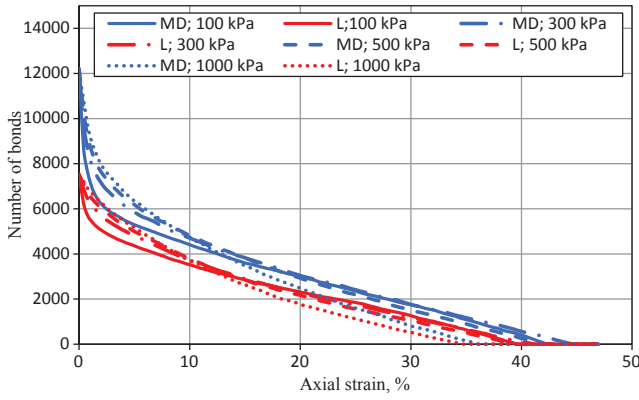


Fig. 9. The effect of confining pressure on the evolution of the number of bonds for loose and medium dense samples ( $\Gamma = 20 \text{ J/m}^2$ ).

bond breakage occurs before the maximum deviator stress is reached.

#### 4.1. Peak strengths

The peak strength data of triaxial compression tests for both the loose and medium dense systems are represented by Mohr-Coulomb strength envelopes in Figs. 10 and 11. Over a range of 100–1000 kPa confining pressures, the envelopes are straight lines almost with the same slope, but slightly different intercepts. The Mohr-Coulomb strength criterion is defined by

$$\sigma_1 - \sigma_3 - 2c' \cos \varphi' - (\sigma_1 + \sigma_3) \sin \varphi' = 0 \quad (14)$$

where  $c'$  is the apparent cohesion, which is a unique function of bond strength and  $\varphi'$  is the so-called angle of internal friction. The internal friction angles of loose system range from  $32.5^\circ - 35.5^\circ$ , while for medium dense system it varies from  $35.1^\circ - 37.8^\circ$ , with average values of  $33.7^\circ$  and  $36.5^\circ$ , respectively. Similar behavior was obtained in laboratory tests reported by Dupas and Pecker [30]; Clough et al. [2]; Acar and El-Tahir [31]. The apparent cohesion was calculated using the average value of internal friction angle for loose and medium dense systems from:

$$c' = \frac{(\sigma_1 - \sigma_3)}{2 \cos \varphi'} - \frac{(\sigma_1 + \sigma_3) \tan \varphi'}{2} \quad (15)$$

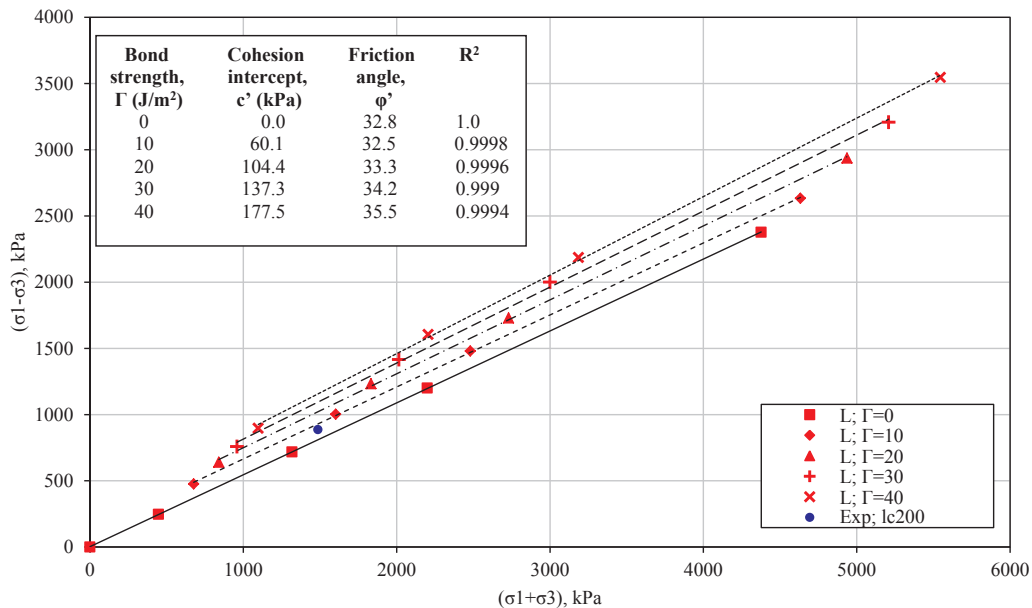


Fig. 10. Mohr-Coulomb strength envelopes for loose sample.

Figs. 10 and 11 show that with increase in bond strength, the apparent cohesion, tensile strength and internal friction angle increase. The same effects have been observed in the experiments on cemented sand by Clough et al. [2]; Lade and Overton [3]; Schnaid et al. [10]; Airey [6]; Wang et Leung [11,12]; Rios et al. [14]. It was observed that there is a smaller apparent cohesion and lower internal friction angle for the loose system compared with the medium dense system. The higher friction angle of the medium dense samples is a result of the initial density. The denser samples have more initial cemented bonds compared with looser samples so, as the amount of cemented bonds increase, the cohesion intercept, tensile strength and friction angle also increase. Clough et al. [2] reported that the density has a significant influence on cemented soil strength, in addition to the nature of the cementing material. The cohesion intercept of uncemented sand for both systems is equal to 0 and therefore their peak strengths are the result of dilation (Coop and Willson [9]), while for the cemented sand it is the result of the cohesive-frictional nature.

Two peak strength data points LC200 (loose sample) and LC500 (medium dense sample) from laboratory triaxial compression tests on sandstone analogue samples by Shabdirova et al. [21] have been added to the Mohr-Coulomb strength envelopes for loose and medium dense samples, respectively. It is shown that the peak strength of LC200 locates between the slopes of  $\Gamma = 0$  and  $10 \text{ J/m}^2$  (Fig. 10), and LC500 locates on the slope of  $\Gamma = 20 \text{ J/m}^2$  (Fig. 11). To find the exact value of the bond strength to be used for comparison with experimental results, a non-linear correlation was obtained between the Mohr-Coulomb shear strength parameter  $c'$  and bond strength  $\Gamma$ , as illustrated in Fig. 12. Superimposed experimental data points indicate that values of  $\Gamma = 6.5 \text{ J/m}^2$  and  $\Gamma = 20 \text{ J/m}^2$  should be used to compare the numerical simulations with the laboratory results for loose and medium dense samples, respectively.

Figs. 13 and 14 show the comparison obtained between the numerical data and laboratory triaxial compression tests at a confining pressure of 300 kPa. It can be seen that the stress-strain responses of the numerical samples were found to be in good agreement with the experimental results at least in terms of the shear strength. However, the numerical samples do not contract as much due to the difference between interface energy and cement (cement bonds are compressible and this is not accounted for in the simple modified JKR bond model). Consequently, the stress-strain curves for the numerical samples are stiffer.



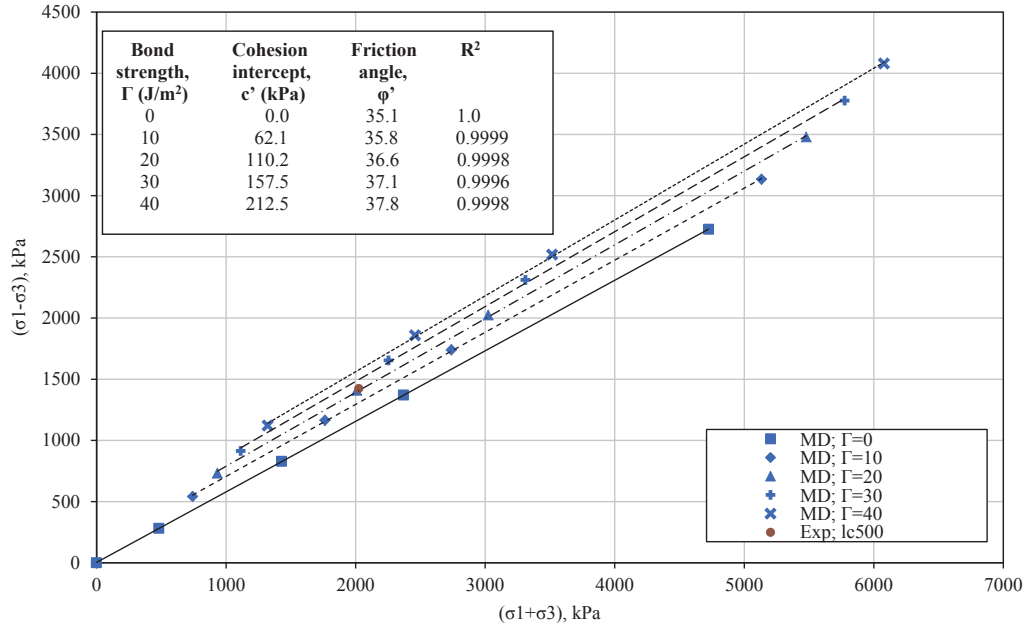


Fig. 11. Mohr-Coulomb strength envelopes for medium dense sample.

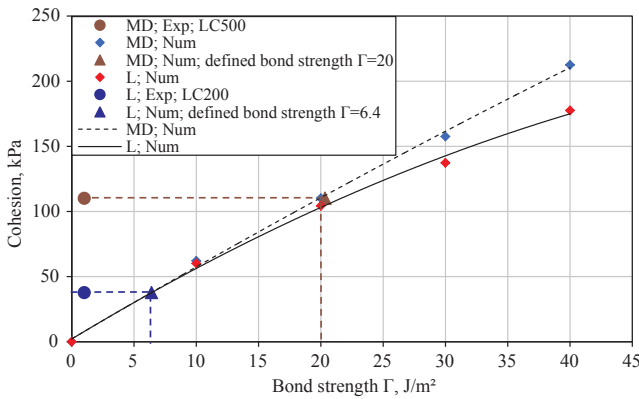


Fig. 12. The correlation between the shear strength parameters and the bond strength for loose and medium dense samples.

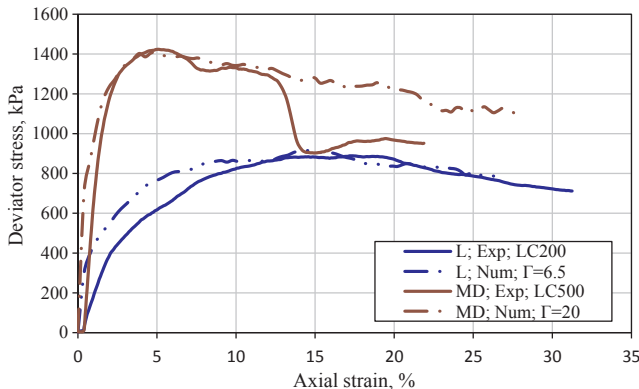


Fig. 13. Comparison of numerical and experimental stress-strain curves for loose and medium dense samples.

#### 4.2. Critical state

Fig. 15 shows the critical state lines (CSL) obtained for both the loose and medium dense systems in the  $e - \ln p'$  plane. The CSL was originally introduced to explain the behaviour of normally consolidated

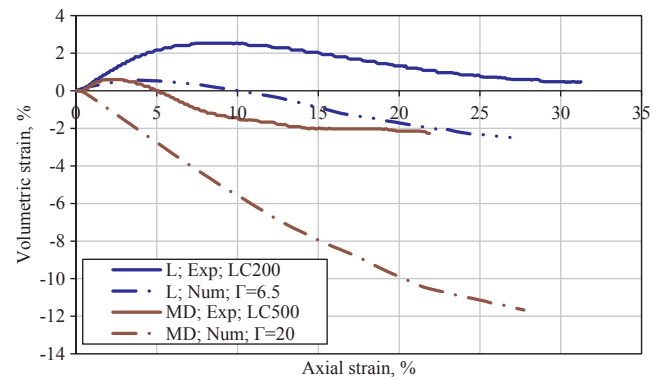


Fig. 14. Comparison of numerical and experimental volume change curves for loose and medium dense samples.

clay, and only a few investigators have used it for cemented sand materials (Airey [6], Coop and Atkinson [5], and Cuccovillo and Coop [8]). Schnaid et al. [10] reported that the complete determination of the critical state in a  $p': q: e$  space presents some experimental difficulties, given the brittle behaviour and the strain localization observed for cemented specimens although the investigation of the critical state line plays a fundamental role in establishing a general theoretical framework for the behaviour of cemented soils.

Coop and Willson [9] suggested that in order to identify the CSL for sands it requires shearing to strains of 30% or more. In this paper, all the triaxial compression simulations were continued to 46% axial strain. It can be seen from Fig. 15 that for a given value of bond strength both the loose and medium dense samples reach the same critical state line. The critical void ratio is independent of the initial density; it increases with increase in bond strength, and decreases with increase in confining pressure. Increasing the bond strength increases the dilation, which leads to a higher critical state void ratio.

Further, the CSL parameters  $e_1$  and  $\lambda$  are obtained using the following equation:

$$e = e_1 - \lambda \ln p' \quad (16)$$

where,  $e -$  is a critical state void ratio,  $e_1$  - is the value of  $e$  corresponding to  $p' = 1$  kPa on the critical state line,  $\lambda$  is the slope of the CSL

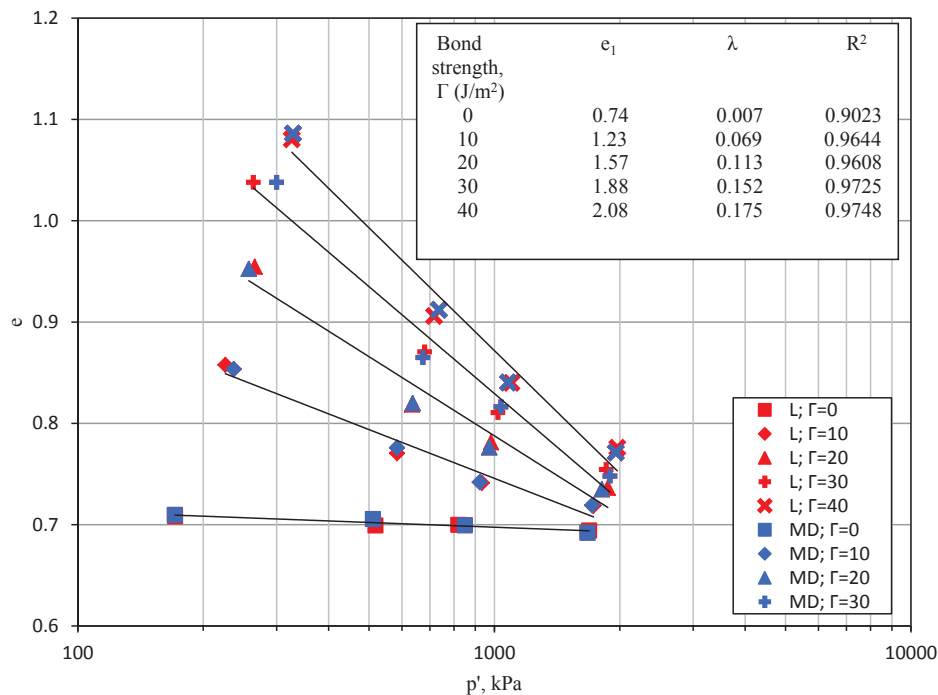


Fig. 15. Critical state line in the  $e - \ln p'$  plane for loose and medium dense samples.

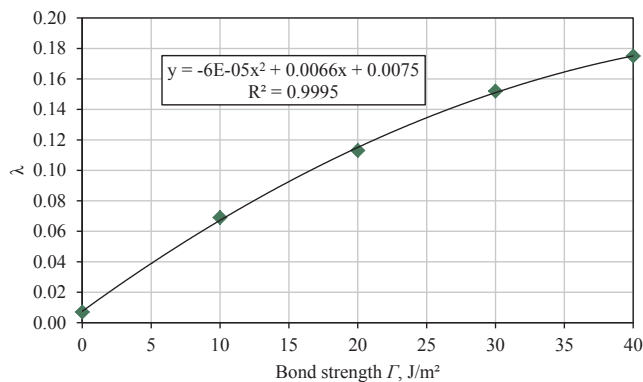


Fig. 16. The correlation between the slope of the CSL in the  $e - \ln p'$  plane and the bond strength for both loose and medium dense samples.

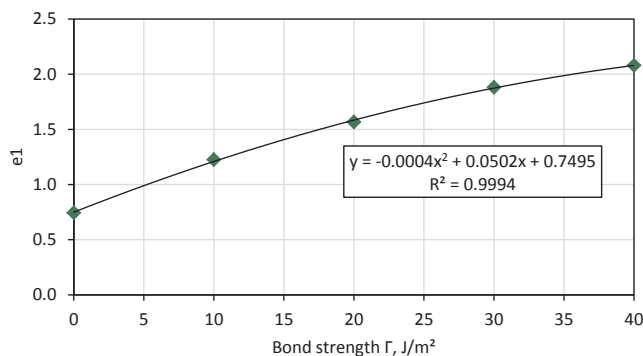


Fig. 17. The correlation between the intercept at 1 kPa of the CSL in the  $e - \ln p'$  plane and the bond strength for both loose and medium dense samples.

in the  $e - \ln p'$  plane. The slope of the CSL (compression index) for both systems range from 0.007 to 0.175, and it increase with increase in bond strength. The non-linear correlations between the CSL parameters  $\lambda$  and  $\Gamma$  and between  $e_1$  and  $\Gamma$ , are shown in Figs. 16 and 17,

respectively.

## 5. Concluding remarks

Three dimensional DEM simulations of triaxial compression tests on loose and medium dense samples have been performed in periodic cells. Material properties of experimental sandstone from the Ustyurt-Buzachi Sedimentary Basin were replicated for the numerical samples. A total of 40 simulations were performed with 5206 frictional elastic spherical particles at different values of confining pressure and bond strength, where in all cases particle rotations were prevented. The results show that the peak strength and initial stiffness increase with increase in bond strength, initial density and confining pressure, and for a higher bond strength and initial density the stress reaches a peak at a lower axial strain. For higher bond strengths the samples exhibit a higher rate of dilation but the volumetric dilation decreases with increasing confining pressure. Less bond breakage occurs for a higher bond strength both for loose and medium dense systems.

The Mohr-Coulomb strength criterion parameters  $c'$  and  $\phi'$  were obtained for both loose and medium dense systems. The bond strength values to be used for comparison with experimental results were identified by correlating the bond strength with the Mohr-Coulomb shear strength parameters. In this way it was shown that the stress-strain responses of the numerical samples were in good agreement with experimental results, at least in terms of the shear strength.

A significant feature of the simulations is that, by using a periodic cell, homogeneous deformation is obtained throughout the test, there is no strain localization. Consequently, strain softening continues to occur until the critical state is reached. As a consequence, the simulations clearly demonstrate that, in principle, the critical state void ratio is a function of the bond strength and that higher bond strengths lead to higher critical state void ratios, due to the higher rate of dilation induced when the bond strength is high.

It has been demonstrated that the simple contact interaction model can be calibrated to obtain stress-strain curves that are in good agreement with experimental data. However, the simple model fails to predict the amount of contraction observed in the laboratory tests. Consequently, in order to model the compressibility and crushability of

cement bonds, it is expected that, in any future work, the contact interaction model of Shen et al [19] will be used.

## Acknowledgments

This research was supported by the EU Project GEO-RAMP (H2020-MSCA-RISE-2014 GA 645665) and by the Nazarbayev University research grant SOE 2015004. The authors gratefully acknowledge Prof. Stefano Utili (Newcastle University) and Dr. Helen Cheng (University College London) for their help during the first author's visits to the UK, Furkhat Khamitov for his contribution and help.

## references

- [1] Bjorlykke K. Petroleum geoscience: from sedimentary environments to rock physics. Springer; 2010.
- [2] Clough GW, Sitar N, Bachus RC, Rad NS. Cemented sands under static loading. *J Geotech Eng Div (ASCE)* 1981;107(6):799–817.
- [3] Lade PV, Overton DD. Cementation effects in frictional materials. *J Geotech Eng* 1989;115:1373–87.
- [4] Leroueil S, Vaughan PR. The general and congruent effects of structure in natural soils and weak rocks. *Geotechnique* 1990;40(3):467–88.
- [5] Coop MR, Atkinson JH. The mechanics of cemented carbonate sands. *Geotechnique* 1993;43(1):53–67.
- [6] Airey DW. Triaxial testing of naturally cemented carbonate soil. *J Geotech Eng (ASCE)* 1993;119(9):1379–98.
- [7] Huang JT, Airey DW. Properties of artificially cemented carbonate sand. *J Geotech Geoenviron Eng* 1998;124(6):492–9.
- [8] Cuccovillo T, Coop MR. On the mechanics of structured sands. *Geotechnique* 1999;49(6):741–60.
- [9] Coop MR, Willson SM. Behaviour of hydrocarbon reservoir sands and sandstones. *J Geotech Geoenviron Eng* 2003;129(11):1010–9.
- [10] Schnaid F, Prietto P, Consoli N. Characterization of cemented sand in triaxial compression. *J Geotech Geoenviron Eng* 2001;127:857–68.
- [11] Wang YH, Leung SC. Characterization of cemented sand by experimental and numerical investigations. *J Geotech Geoenviron Eng* 2008;134(7):992–1004.
- [12] Wang YH, Leung SC. A particulate-scale investigation of cemented sand behaviour. *Canad Geotech J* 2008;45:29–44.
- [13] Collins BD, Sitar N. Stability of steep slopes in cemented sands. *J Geotech Geoenviron Eng* 2011;137(1):43–51.
- [14] Rios S, Viana da Fonseca A, Baudet BA. On the shearing behaviour of an artificially cemented soil. *Acta Geotech* 2014;9:2158–226.
- [15] Cundall PA, Strack ODL. A discrete numerical model for granular assemblies. *Geotechnique* 1979;29(1):47–65.
- [16] Jung JW, Santamarina JC, Soga K. Stress-strain response of hydrate-bearing sands: numerical study using discrete element method simulations. *J Geophys Res* 2012;117:1–12.
- [17] Utili S, Nova R. DEM analysis of bonded granular geomaterials. *Int J Numer Anal Meth Geomech* 2008;32(17):1997–2031.
- [18] Obermayr M, Dressler K, Vrettos C, Eberhard P. A bonded-particle model for cemented sand. *Comput Geotech* 2013;49:299–313.
- [19] Shen ZF, Jiang M, Thornton C. DEM simulations of bonded granular material. Part I: Contact model and application to cemented sand. *Comput Geotech* 2016;75:192–209.
- [20] Shen ZF, Jiang M. DEM simulations of bonded granular material. Part II: extension to grain-coating type methane hydrate bearing sand. *Comput Geotech* 2016;75:225–43.
- [21] Shabdirova AD, Bissekova Z, Minh NH, Kim JR. Sample preparation method of clay-rich sandstone analogue reservoir in Kazakhstan. In: *Proceedings of the 50th rock mechanics/geomechanics symposium*, Houston, Texas; 2016.
- [22] Rakhimzhanova AK, Khamitov FA, Minh NH, Thornton C. 3D DEM simulations of triaxial compression tests of cemented sandstone. In: *Proceedings of IS Atlanta 2018 symposium on geomechanics from micro to macro in research and practice*, Atlanta, USA; 2018. [in press].
- [23] Thornton C. Granular dynamics, contact mechanics and particle system simulations – a DEM study. Particle technology series, vol. 24. New York USA: Springer; 2015.
- [24] Hertz H. Über die Berührung fester elastischer Körper. *Journal für die reine und angewandte. Mathematik* 1881;92:156–71.
- [25] Mindlin RD. Compliance of elastic bodies in contact. *Trans ASME J Appl Mech* 1949;16:259–68.
- [26] Johnson KL, Kendall K, Roberts AD. Surface energy and the contact of elastic solids. *Proc R Soc Lond A* 1971;324(1558):301–13.
- [27] Johnson KL. Adhesion at the contact of solids. In: Koiter WT, editor. *Theoretical and applied mechanics*. In: *Proceedings of the 4th IUTAM Congress*; 1976. p. 133–43.
- [28] Calvetti F, Nova R. Micromechanical approach to slope stability analysis. *Degradation and instabilities in geomaterials*. Berlin, Germany: Springer; 2004. p. 235–54.
- [29] Thornton C. Numerical simulations of deviatoric shear deformation of granular media. *Geotechnique* 2000;50(1):43–53.
- [30] Dupas JM, Pecker A. Static and dynamic properties of sand-cement. *J Geotech Eng Div (ASCE)* 1979;105(5):419–36.
- [31] Acar YB, El-Tahir AE. Low strain dynamic properties of artificially cemented sand. *J Geotech Eng* 1986;112(11):1001–15.